

Research Article

Numerical Modeling of Wave-Current Flow around Cylinders Using an Enhanced Equilibrium Bhatnagar-Gross-Krook Scheme

Liming Xing ¹, Haifei Liu ^{1,2}, Yu Ding,¹ and Wei Huang³

¹The Key Laboratory of Water and Sediment Sciences of Ministry of Education, School of Environment, Beijing Normal University, Beijing 100875, China

²State Key Laboratory of Hydraulics and Mountain River Protection, College of Water Resource and Hydropower, Sichuan University, Chengdu 610065, China

³State Key Laboratory of Simulation and Regulation of Water Cycle in River Basin, China Institute of Water Resources and Hydropower Research, Beijing 100038, China

Correspondence should be addressed to Haifei Liu; haifei.liu@bnu.edu.cn

Received 28 June 2017; Revised 11 January 2018; Accepted 23 January 2018; Published 15 February 2018

Academic Editor: Salvatore Alfonzetti

Copyright © 2018 Liming Xing et al. This is an open access article distributed under the Creative Commons Attribution License, which permits unrestricted use, distribution, and reproduction in any medium, provided the original work is properly cited.

Flow around cylinders is a classic issue of fluid mechanics and it has great significance in engineering fields. In this study, a two-dimensional hydrodynamic lattice Boltzmann numerical model is proposed, coupling wave radiation stress, bed shear stress, and wind shear stress, which is able to simulate wave propagation of flow around cylinders. It is based on shallow water equations and a weight factor is applied for the force term. An enhanced equilibrium Bhatnagar-Gross-Krook (BGK) scheme is developed to treat the wave radiation stress term in collision step. This model is tested and verified by two cases: the first case is the flow around a single circular cylinder, where the flow is driven by current, wave, or both wave and current, respectively, and the second case is the solitary waves moving around cylinders. The results illustrate the correctness of this model, which could be used to analyze the detailed flow pattern around a cylinder.

1. Introduction

The phenomena of flow around cylinders, which represent blunt bodies, widely exist in aviation, mechanical, and environmental engineering. In recent years, an increasing number of problems about complex flow around cylinders have been raised with the development of coastal engineering projects. Therefore, this topic attracts much attention among researchers.

Flow around cylinders is a classic and complicated problem. The cross section is contracted, the velocity increases, and the pressure decreases along the path when the flow encounters cylinders. The separation of the boundary layer is formed around cylinders due to the viscous force, which is called the flow around cylinders. Additionally, cylinders are non-streamline objects, which influence the characteristics of

flow around cylinders by many factors, such as the Reynolds number, the surface roughness, the turbulence intensity, and the cylinder size. All these lead to the complexity of flow around cylinders. The wave is one of the most common movement forms in water, and it is worth studying wave motion in shipping, coastal, and ocean engineering. Therefore, the research of wave propagation around cylinders is complicated, but significant.

With the development of the fluid mechanics theory and the continuous updating of computer equipment, computational fluid dynamics has been greatly developed and numerical simulation became an important tool in research. Saiki and Biringen [1] introduced a virtual boundary technique to simulate uniform flows around cylinders, and the oscillations caused by this method can be attenuated by high-order finite differences. Based on this, Lima E Silva et

al. [2] proposed the physical virtual model in which this immersed boundary was represented with a finite number of Lagrangian points, distributed over the solid-fluid interface. Ofengeim and Drikakis [3] presented numerical research on the interaction of plane blast waves and a cylinder, revealing that the blast-wave duration significantly influenced the unsteady flow around the cylinder. Breuer [4] computed the turbulent flow around a cylinder ($Re = 3900$) via large eddy simulation. Meneghini et al. [5] used a fractional step method to simulate laminar flows between two cylinders. Hu et al. [6] built a fully nonlinear potential model based on a finite element method to investigate the wave motion around a moving cylinder, and it provided certain important features that were absent in the linear theory. Wu and Shu [7] proposed a local domain-free discretization method that is able to simulate flow around an oscillating cylinder easier due to its advantage of handling the boundary. Claus and Phillips [8] used spectral/hp element methods to study the flow around a confined cylinder. The nonconforming spectral element method and adaptive meshes method were tested by Hsu et al. [9], demonstrating its feasibility on curve surfaces of cylinder.

The lattice Boltzmann method (LBM) is a promising numerical simulation method of recent decades. Compared to traditional methods, LBM has many advantages: the algorithm is simple; it can deal with complicated boundary conditions; and it is suitable for parallel processing. These superiorities lead to wide usage of LBM in many research fields. Ginzburg and D’Humières [10] introduced a new kind of boundary conditions, improving the accuracy close to the quasianalytical reference solution. Jiménez-Hornero et al. [11] used LBM to simulate the turbulent flow structure in an open channel with the influence of vegetation. Liu et al. [12] established a two-dimensional multiblock lattice Boltzmann model for solute transport in shallow water flows. Based on the Chapman-Enskog process, Liu and Zhou [13] proposed a lattice Boltzmann model to simulate the wetting-drying front in shallow flows.

At the same time, many scholars have investigated the flow around cylinders based on the LBM. However, most studies are related to the heat transfer around cylinders. Yan and Zu [14] presented a numerical strategy to handle curved and moving boundaries for simulating viscous fluid around a rotating isothermal cylinder with heat transfer. Rabienataj Darzi et al. [15] used the LBM to analyze mixed convection flow and heat transfer between two hot cylinders. However, up to now, there is no LBM model for wave-current flow around cylinders.

In this study, considering wave-current interaction, a two-dimensional hydrodynamic numerical model is developed based on the LBM. The model couples three types of stresses, including wave radiation stress, wind shear stress, and bed shear stress. Meanwhile, an enhanced local equilibrium function is developed to treat the wave radiation stress. It is used to simulate the propagation of waves in the flow around cylinders, and then two classic examples are used for validation, which can provide characteristics of flow around cylinders.

2. Methodology

2.1. Governing Equations. The two-dimensional shallow water equations including the continuity equation and momentum equation can be written in a tensor form as

$$\begin{aligned} \frac{\partial h}{\partial t} + \frac{\partial(hu_j)}{\partial x_j} &= 0, \\ \frac{\partial(hu_i)}{\partial t} + \frac{\partial(hu_i u_j)}{\partial x_j} &= -g \frac{\partial}{\partial x_i} \left(\frac{h^2}{2} \right) + \nu \frac{\partial^2(hu_i)}{\partial x_j \partial x_j} \\ &\quad - g \bar{h} \frac{\partial Z_b}{\partial x_j} + \frac{\partial S_{ij}}{\partial x_j} + F_i, \end{aligned} \quad (1)$$

where the subscripts i and j represent the space direction indices and the Einstein summation convention is used; x_j represents the Cartesian coordinate, taking x , y , and z in turn; u_j represents the velocity component which takes u and v corresponding to that in x and y and directions, respectively. h represents the water depth; t represents the time; ν represents the kinematic viscosity; Z_b represents the bed height of the datum plane and F_i represents the force term and defined as

$$F_i = \frac{\tau_{wi}}{\rho} - \frac{\tau_{bi}}{\rho}, \quad (2)$$

where τ_{wi} represents the wind shear stress and τ_{bi} represents the bed shear stress.

Wave Radiation Stress (S_{ij}). Longuet-Higgins and Stewart [16] defined the difference between the time-average momentum value and the static water pressure on the water column per unit area, known as the wave radiation stress.

In (3), the wave radiation stresses S_{xx} , S_{xy} , S_{yx} , and S_{yy} are determined via local wave parameters. The wave radiation stress along the direction of wave propagation is $S_x = E(2C_g/C - 1/2)$, and the lateral one is $S_y = E(C_g/C - 1/2)$, where $E = (1/8)\rho g H_w^2$, C is wave velocity, C_g represents the group velocity, and H_w represents the wave height. The conversion is conducted in the Cartesian coordinate system [17]:

$$\begin{aligned} S_{xx} &= S_x \cos^2 \theta - S_y \sin^2 \theta, \\ S_{yy} &= S_x \sin^2 \theta - S_y \cos^2 \theta, \\ S_{xy} &= S_{yx} = S_x \sin 2\theta \cos \theta - S_y \cos \theta \sin \theta, \end{aligned} \quad (3)$$

where θ represents the angle between the wave direction and the x -axis.

Bed Shear Stress (τ_{bi}). Bed shear stress (τ_{bi}) is generated by the wave-current interaction in the i direction, calculated as follows [18]:

$$\begin{aligned} \tau_{bi} &= \rho C_b u_i \sqrt{u_j u_j} + \frac{\pi \rho}{8} f_w \sqrt{u_{wj} u_{wj}} u_{wj} \\ &\quad + \frac{F_B \rho}{\pi} \sqrt{2} (C_b f_w)^{1/2} \sqrt{u_{wj} u_{wj}} u_{wj}, \end{aligned} \quad (4)$$

in which C_b represents the bed friction coefficient, which may be either constant or calculated from $C_b = g/C_z^2$, where C_z represents the Chezy coefficient given based on the Manning coefficient n_b ,

$$C_z = \frac{h^{1/6}}{n_b}; \quad (5)$$

u_{wi} represents the wave bottom frictional velocity; F_B represents the wave-current influence factor, which is equal to 0.917 for the waves and currents are in the same direction, -0.1983 for perpendicular relation and 0.359 for other angles [19]; and f_w represents the wave friction factor, which is from 0.006 to 0.001 in practice [20].

Wind Shear Stress (τ_{wi}). Wind shear stress (τ_{wi}) is usually expressed as

$$\tau_{wi} = \rho_a C_w u_{wi} \sqrt{u_{wj} w_{wj}}, \quad (6)$$

where ρ_a is the density of air; C_w is the resistance coefficient; and u_{wi} is the component of the wind velocity in i direction.

2.2. Lattice Boltzmann Method. On account of the lattice Boltzmann method with a D2Q9 lattice, an enhanced equilibrium BGK Scheme is developed in this paper. The wave radiation stress S_{ij} is treated in local equilibrium function at collision step.

The discrete evolution process in the LBM with the enhanced force term [12, 21] can be written as

$$\begin{aligned} & f_\alpha(X + e_\alpha \Delta t, t + \Delta t) - f_\alpha(X, t) \\ &= -\frac{1}{\tau} (f_\alpha - f_\alpha^{\text{eq}}) - 3\Delta t \omega_\alpha e_{\alpha j} \frac{gh}{e^2} \frac{\partial Z_b}{\partial x_j} + \Delta t F_\alpha, \end{aligned} \quad (7)$$

where the external force term can be written as

$$F_\alpha = 3\omega_\alpha \frac{1}{e^2} e_{\alpha i} \left(\frac{\tau_{wi}}{\rho} - \frac{\tau_{bi}}{\rho} \right), \quad (8)$$

where ω_α represents the weight factor: $\omega_\alpha = 4/9$ for $\alpha = 0$; $\omega_\alpha = 1/9$ for $\alpha = 1, 3, 5, 7$; $\omega_\alpha = 1/36$ for $\alpha = 2, 4, 6, 8$. f_α represents the distribution function of particles; f_α^{eq} represents the local equilibrium distribution function; Δt represents the time step; τ represents the single relaxation time; and e_α represents the velocity vector of a particle in the α link.

For the D2Q9 lattice shown in Figure 1, each particle moves one lattice at its direction. The velocity of each particle is defined by

$$e_\alpha = \begin{cases} (0, 0) & \alpha = 0, \\ e \left[\cos \frac{(\alpha-1)\pi}{4}, \sin \frac{(\alpha-1)\pi}{4} \right] & \alpha = 1, 3, 5, 7, \\ \sqrt{2}e \left[\cos \frac{(\alpha-1)\pi}{4}, \sin \frac{(\alpha-1)\pi}{4} \right] & \alpha = 2, 4, 6, 8, \end{cases} \quad (9)$$

where $e = \Delta x / \Delta t$ and Δx is the lattice size.

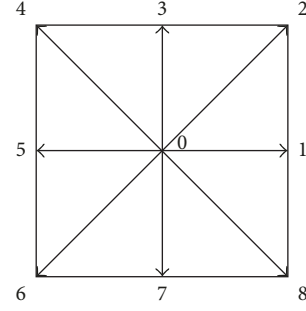


FIGURE 1: D2Q9 lattice.

An equilibrium distribution function f_α^{eq} can be expressed as

$$f_\alpha^{\text{eq}} = A_\alpha + B_\alpha e_{\alpha i} u_i + C_\alpha e_{\alpha i} e_{\alpha j} u_i u_j + D_\alpha u_i u_i. \quad (10)$$

Therefore, the equilibrium distribution function can be written as

$$f_\alpha^{\text{eq}} = \begin{cases} A_0 + D_0 u_i u_i & \alpha = 0, \\ \bar{A} + \bar{B} e_{\alpha i} u_i + \bar{C} e_{\alpha i} e_{\alpha j} u_i u_j + \bar{D} u_i u_i & \alpha = 1, 3, 5, 7, \\ \tilde{A} + \tilde{B} e_{\alpha i} u_i + \tilde{C} e_{\alpha i} e_{\alpha j} u_i u_j + \tilde{D} u_i u_i & \alpha = 2, 4, 6, 8, \end{cases} \quad (11)$$

where there must be

$$\begin{aligned} A_1 &= A_3 = A_5 = A_7 = \bar{A}, \\ A_2 &= A_4 = A_6 = A_8 = \tilde{A} \end{aligned} \quad (12)$$

due to symmetry.

Moreover, the local equilibrium distribution function must satisfy the following three conditions:

$$\begin{aligned} \sum_\alpha f_\alpha^{\text{eq}}(X, t) &= h(X, t), \\ \sum_\alpha e_{\alpha i} f_\alpha^{\text{eq}}(X, t) &= h(X, t) u_i(X, t), \\ \sum_\alpha e_{\alpha i} e_{\alpha j} f_\alpha^{\text{eq}}(X, t) &= \frac{1}{2} g h^2(X, t) \delta_{ij} - S_{ij} \\ &\quad + h(X, t) u_i(X, t) u_j(X, t). \end{aligned} \quad (13)$$

Hence, the relations among A_0 , \bar{A} , and \tilde{A} are

$$\begin{aligned} A_0 + 4\bar{A} + 4\tilde{A} &= h, \\ 2e^2\bar{A} + 4e^2\tilde{A} &= \frac{1}{2} g h^2 - S_{ij}, \\ \bar{A} &= 4\tilde{A}. \end{aligned} \quad (14)$$

We can obtain

$$\bar{B} = \frac{h}{3e^2},$$

$$\bar{C} = \frac{h}{4e^2},$$

$$\bar{D} = -\frac{h}{6e^2},$$

$$\tilde{B} = \frac{h}{12e^2},$$

$$\tilde{C} = \frac{h}{8e^2},$$

$$\tilde{D} = -\frac{h}{24e^2}.$$

(15)

Therefore, the enhanced equilibrium distribution function f_α^{eq} is

$$f_\alpha^{\text{eq}} = \begin{cases} h - \frac{5gh^2}{6e^2} + \frac{5S_{ij}}{3e^2} - \frac{2h}{3e^2}u_i u_i, & \alpha = 0, \\ \frac{gh^2}{6e^2} - \frac{S_{ij}}{3e^2} + \frac{h}{3e^2}e_{\alpha i}u_i + \frac{h}{2e^4}e_{\alpha i}e_{\alpha j}u_i u_j - \frac{h}{6e^2}u_i u_i, & \alpha = 1, 3, 5, 7, \\ \frac{gh^2}{24e^2} - \frac{S_{ij}}{12e^2} + \frac{h}{12e^2}e_{\alpha i}u_i + \frac{h}{8e^4}e_{\alpha i}e_{\alpha j}u_i u_j - \frac{h}{24e^2}u_i u_i, & \alpha = 2, 4, 6, 8. \end{cases} \quad (16)$$

2.3. Recovery of Wave-Current Coupling Equations. The recover deductions are following the Chapman-Enskog procedure.

Based on (7), assuming Δt is small, taking Taylor expansion in time and space around point (X, t) leads to

$$\begin{aligned} f_\alpha(X + e_\alpha \Delta t, t + \Delta t) &= f_\alpha(X, t) + \Delta t \left(\frac{\partial}{\partial t} + e_{\alpha j} \frac{\partial}{\partial x_j} \right) f_\alpha(X, t) \\ &+ \frac{1}{2} \Delta t^2 \left(\frac{\partial}{\partial t} + e_{\alpha j} \frac{\partial}{\partial x_j} \right)^2 f_\alpha(X, t) + o(\Delta t^2). \end{aligned} \quad (17)$$

From Chapman-Enskog expansion, we have

$$f_\alpha = f_\alpha^{(0)} + \Delta t f_\alpha^{(1)} + \Delta t^2 f_\alpha^{(2)} + o(\Delta t^2). \quad (18)$$

Substitution of (17) and (18) into (7), one can obtain

$$\begin{aligned} \Delta t \left(\frac{\partial}{\partial t} + e_{\alpha j} \frac{\partial}{\partial x_j} \right) (f_\alpha^{(0)} + \Delta t f_\alpha^{(1)} + \Delta t^2 f_\alpha^{(2)}) &+ \frac{1}{2} \Delta t^2 \left(\frac{\partial}{\partial t} + e_{\alpha j} \frac{\partial}{\partial x_j} \right)^2 (f_\alpha^{(0)} + \Delta t f_\alpha^{(1)} + \Delta t^2 f_\alpha^{(2)}) \\ &= -\frac{1}{\tau} (\Delta t f_\alpha^{(1)} + \Delta t^2 f_\alpha^{(2)}) - 3\Delta t \omega_\alpha e_{\alpha j} \frac{g\bar{h}}{e^2} \frac{\partial Z_b}{\partial x_j} \\ &+ \Delta t F_\alpha. \end{aligned} \quad (19)$$

To order Δt , it is

$$\begin{aligned} \left(\frac{\partial}{\partial t} + e_{\alpha j} \frac{\partial}{\partial x_j} \right) f_\alpha^{(0)} &= -\frac{1}{\tau} f_\alpha^{(1)} - 3\omega_\alpha e_{\alpha j} \frac{g\bar{h}}{e^2} \frac{\partial Z_b}{\partial x_j} \\ &+ F_\alpha. \end{aligned} \quad (20)$$

To order Δt^2 , it is

$$\begin{aligned} \left(\frac{\partial}{\partial t} + e_{\alpha j} \frac{\partial}{\partial x_j} \right) f_\alpha^{(1)} + \frac{1}{2} \left(\frac{\partial}{\partial t} + e_{\alpha j} \frac{\partial}{\partial x_j} \right)^2 f_\alpha^{(0)} \\ = -\frac{1}{\tau} f_\alpha^{(2)}. \end{aligned} \quad (21)$$

Substitution of (20) into (21), we have

$$\begin{aligned} \left(1 - \frac{1}{2\tau} \right) \left(\frac{\partial}{\partial t} + e_{\alpha j} \frac{\partial}{\partial x_j} \right) f_\alpha^{(1)} \\ = -\frac{1}{2} \left(\frac{\partial}{\partial t} + e_{\alpha j} \frac{\partial}{\partial x_j} \right) \left(-3\omega_\alpha e_{\alpha j} \frac{g\bar{h}}{e^2} \frac{\partial Z_b}{\partial x_j} + F_\alpha \right) \\ - \frac{1}{\tau} f_\alpha^{(2)}. \end{aligned} \quad (22)$$

Taking $\sum [(20) + \Delta t \times (22)]$ about α provides

$$\begin{aligned} \frac{\partial}{\partial t} \left(\sum_\alpha f_\alpha^{(0)} \right) + \frac{\partial}{\partial x_j} \left(\sum_\alpha e_{\alpha j} f_\alpha^{(0)} \right) \\ = -\varepsilon \frac{1}{12e^2} \frac{\partial}{\partial x_j} \left(\sum_\alpha e_{\alpha j} e_{\alpha k} F_k \right). \end{aligned} \quad (23)$$

Taking $\sum e_{\alpha i} [(20) + \Delta t \times (22)]$ about α provides

$$\begin{aligned} \frac{\partial}{\partial t} \left(\sum_\alpha e_{\alpha j} f_\alpha^{(0)} \right) + \frac{\partial}{\partial x_j} \left(\sum_\alpha e_{\alpha j} e_{\alpha k} f_\alpha^{(0)} \right) \\ + \Delta t \left(1 - \frac{1}{2\tau} \right) \frac{\partial}{\partial x_j} \left(\sum_\alpha e_{\alpha j} e_{\alpha k} f_\alpha^{(1)} \right) \\ = \left(-g\bar{h} \frac{\partial Z_b}{\partial x_j} + F_i \right) \delta_{ij}. \end{aligned} \quad (24)$$

TABLE 1: The flow variables and wave parameters.

Test	u_0 (m/s)	v_0 (m/s)	Wave period (s)	Wave amplitude (m)
1	1	0	-	-
2	0	0	0.5	0.1
3	1	0	0.5	0.1

According to the law of conservation of mass, we know

$$\sum_{\alpha} f_{\alpha}(X, t) = \sum_{\alpha} f_{\alpha}^{\text{eq}}(X, t). \quad (25)$$

If the center-scheme for the force term is applied, evaluation of the other terms in the above equations using (13) and (25) simplifies (23) and (24) and obtains

$$\begin{aligned} \frac{\partial h}{\partial t} + \frac{\partial(hu_j)}{\partial x_j} &= 0 \\ \frac{\partial(hu_i)}{\partial t} + \frac{\partial(hu_i hu_j)}{\partial x_j} &= -g \frac{\partial}{\partial x_i} \left(\frac{h^2}{2} \right) - \frac{\partial}{\partial x_j} \Lambda_{ij} - g \bar{h} \frac{\partial Z_b}{\partial x_j} + \frac{\partial S_{ij}}{\partial x_j} + F_i, \end{aligned} \quad (26)$$

with

$$\begin{aligned} \Lambda_{ij} &= \frac{\Delta t}{2\tau} (2\tau - 1) \sum_{\alpha} e_{\alpha i} e_{\alpha j} f_{\alpha}^{(1)} \\ &\approx -\nu \left[\frac{\partial(hu_i)}{\partial x_i} + \frac{\partial(hu_j)}{\partial x_i} \right]. \end{aligned} \quad (27)$$

Substitution of (27) into (26) leads to the following equations which were referred to as wave-current coupling equations (1).

3. Numerical Tests

3.1. Wave-Current Flow around a Circular Cylinder. This model is built based on the verified LBM hydrodynamic model [22]. The layout diagram of the channel is shown in Figure 2. The length is 7 m, and the width is 2 m. The bottom is flat and a solid cylinder with a 0.12 m radius is located at 2 m, 1 m. The initial water depth is 1 m and the flows go from the left to the right. The computational domain is divided by 140×40 computational grids. The time step is 0.01 s.

This case includes three different tests, which are driven by currents, by waves, and by both wave and current, respectively. The flow variables and wave parameters of three types situations are shown in Table 1 (u_0 is initial horizontal velocity and v_0 is initial vertical velocity).

Test 1 (driven by the current). It can be seen that the water depth and flow velocity obviously varied due to the presence of the middle column (see Figure 3).

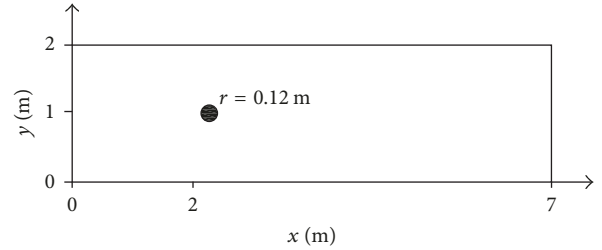


FIGURE 2: The layout sketch of the channel.

When the flow encounters the cylinder, it passes around and a weak area emerges just behind the cylinder, where the circulation and a drop of water surface can be found.

Test 2 (driven by the wave). The initial water is still and a wave maker is set at the inlet, where the incident waves are parallel generated in the x -axis. The water depth is intuitively depicted in Figure 4, where one can find regular wave propagation although there is a deformation caused by the cylinder.

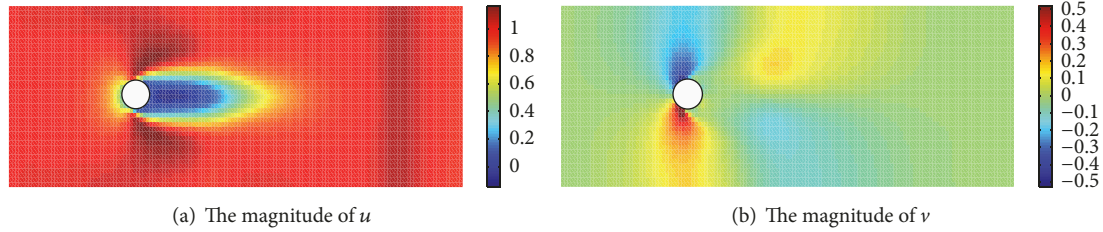
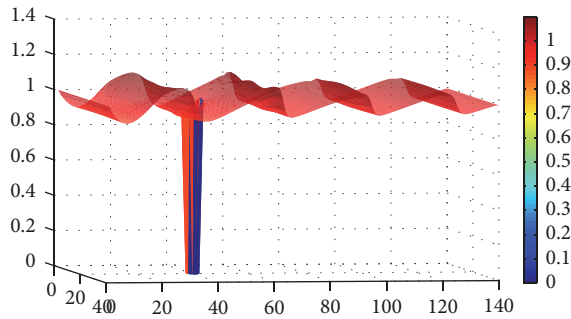
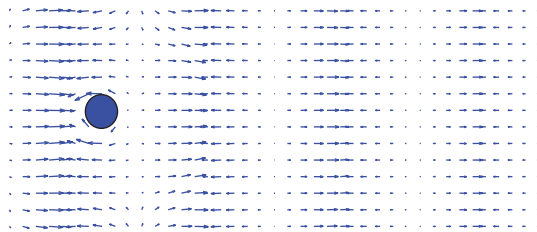
In terms of the longitudinal velocity u , it is not always positive, as the flow is only driven by the wave (see Figures 4 and 5). This phenomenon is further described in Figure 6.

Test 3 (driven by both wave and current). Under the interaction effects of waves and currents, the wave run-up is pushed higher than before (see Figures 7 and 8), and the deformation process is more apparent (see Figure 9).

To illustrate the effects of currents and waves, the comparisons of the velocity u and the water depth h are plotted in Figures 10 and 11, respectively. It can be found that the wave-current interaction is not a simple superposition of waves and currents, and furthermore, wave-current interaction effects are greater than summation of these two effects separately.

3.2. Solitary Waves around Cylinders. This case is a classic cylinder model that has been simulated by many researchers before [23, 24]. In this section, a solitary wave around a cylinder is simulated first. The whole water channel is 60 m long and 30 m wide, and there is a circular cylinder with $R = 1.5875$ m in the center of the channel. The initial solitary wave with amplitude of 0.4 m is incident from left. Lattice size is 0.4 m, and the time step is 0.01 s.

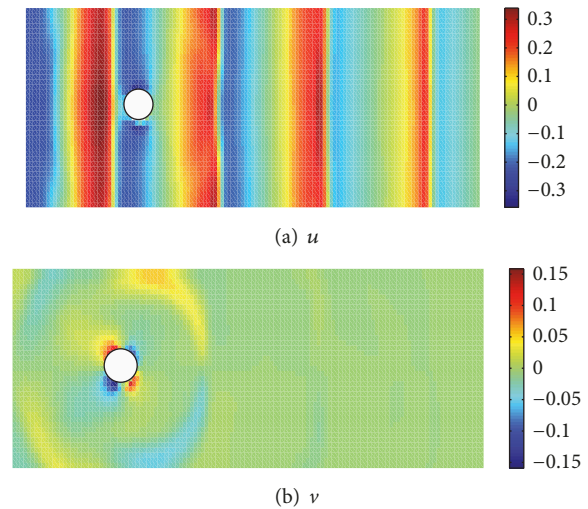
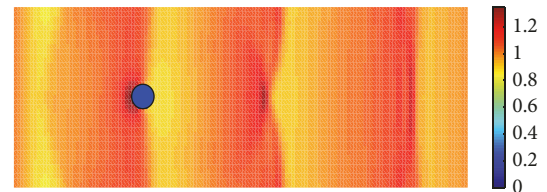
Figure 12 shows the plots of three-dimensional perspective view of water surface at $t = 8.7$ s and 16 s. The solitary wave climbs up and a sequence of significant disperse waves after initial wave encountering the cylinder can be observed. At $t = 16$ s, the solitary wave is about to propagate out of the area. At the same time, disperse waves are fully developed

FIGURE 3: x, y direction of the velocity ($t = 3$ s).FIGURE 4: Three-dimensional water depth diagram ($t = 3$ s).FIGURE 5: Velocity vector diagram ($t = 3$ s).

to cover almost all the channel behind the frontal wave. The results are consistent with previous research [23].

Furthermore, a solitary wave around four cylinders is simulated. The simulation is conducted in an area of constant water depth (1 m), being 60 m long and 40 m wide. The distance between the centers of any two adjacent cylinders is 7.17 m, and the radius of four cylinders is the same with 2 m (see Figure 13). The whole domain is divided by 150×100 computational grids. The time step is 0.01 s.

Figure 14 is the three-dimensional water depth of the wave around four cylinders at different times. The climbing up of water on the first cylinder can be observed at $t = 7$ s. At $t = 9$ s, the solitary wave encounters two middle cylinders and then runs up the front sides. Furthermore, a circular back disperse wave begins to turn up and propagates along the channel. The height of the middle part of the solitary wave decreases significantly due to obstruction of the frontal cylinder. The solitary wave encounters the rear cylinder at $t = 10.5$ s. The results show that the back disperse waves induced by the frontal cylinder form a circular wave pattern propagating towards the left open boundary. At the same time, the circular disperse waves, emerging from the two

FIGURE 6: The magnitude of u and v ($t = 3$ s).FIGURE 7: The magnitude of water surface ($t = 3$ s).

middle cylinders, are also expanded. Due to the complicated interactions between waves and cylinders, the diffracted wave patterns become fully irregular in the domain at $t = 16$ s. The results of the proposed model agree well with the work conducted by Zhong and Wang [23].

4. Conclusion

This paper proposes a two-dimensional hydrodynamic model to investigate the wave-current interaction around cylinders. The lattice Boltzmann method was used to discretize the mathematical model in numerical simulation. A BKG scheme with an enhanced equilibrium is used to treat the wave radiation stress. The numerical results of both cases are in good agreement with practicalities and previous studies, demonstrating that this new model is able to produce reliable results for studying cylinders problems.

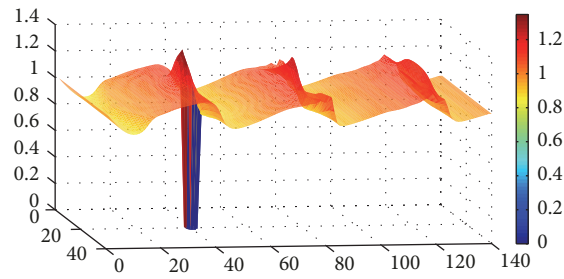
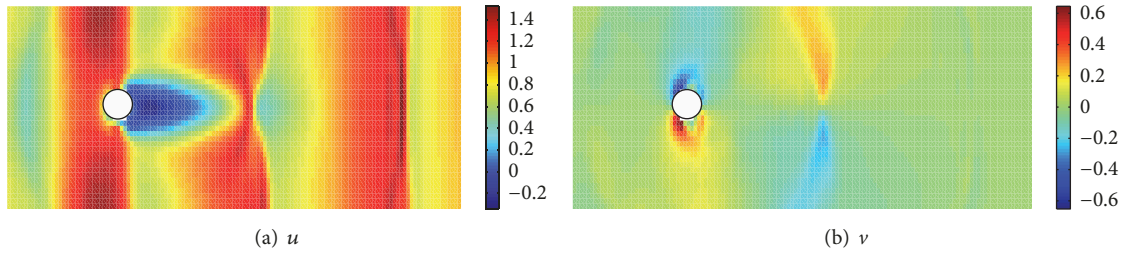


FIGURE 8: Three-dimensional water depth diagram ($t = 3$ s).



(a) u

(b) v

FIGURE 9: The magnitude of u and v ($t = 3$ s).

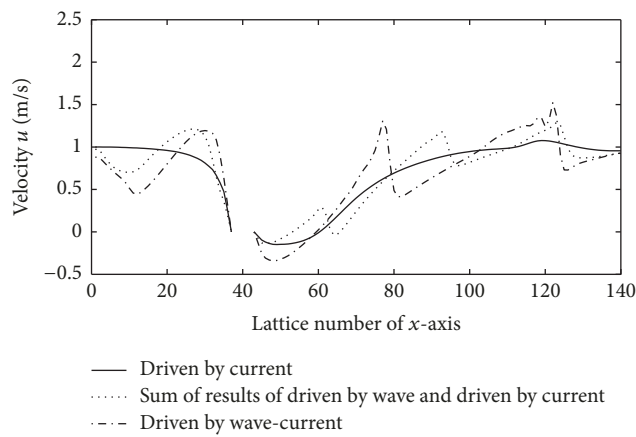


FIGURE 10: Comparison of u ($y = 20$, $t = 3$ s).

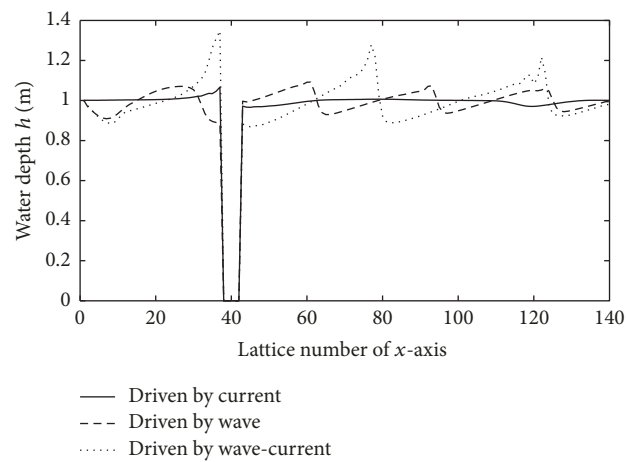


FIGURE 11: Comparison of h ($y = 20$, $t = 3$ s).

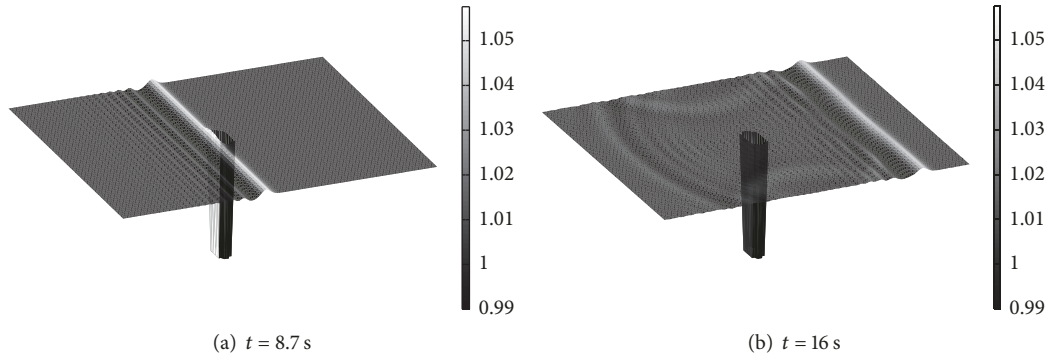


FIGURE 12: The plots of three-dimensional perspective view of water surface.

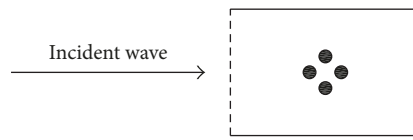


FIGURE 13: The layout of the channel.

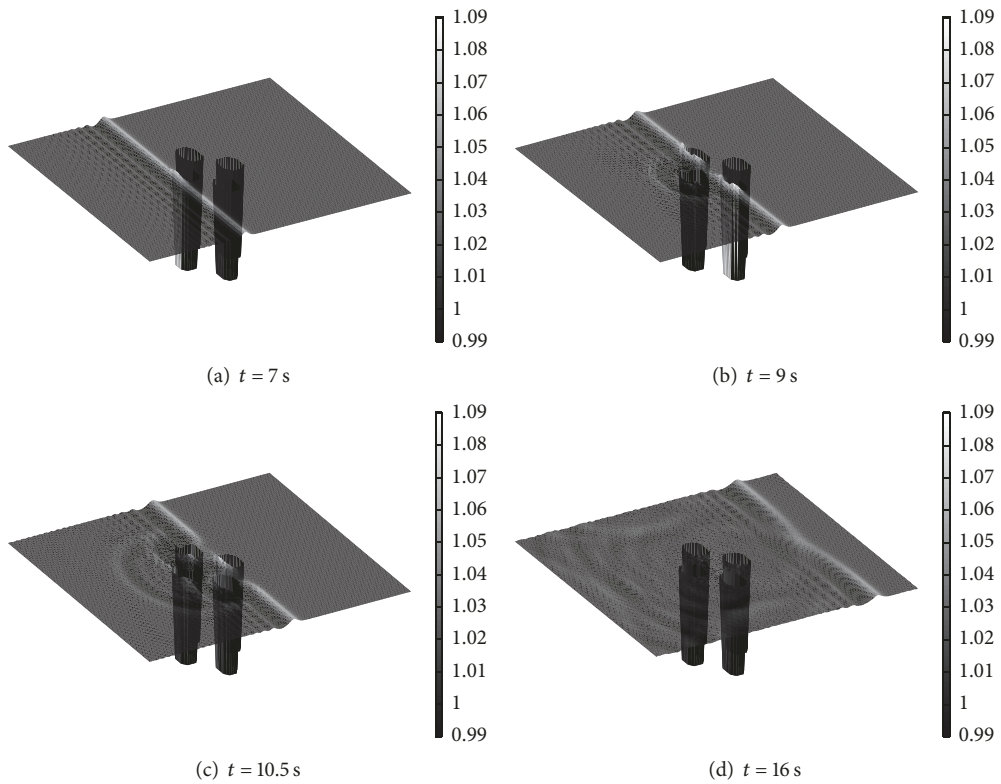


FIGURE 14: The plots of three-dimensional perspective view of water surface.

Conflicts of Interest

The authors declare that there are no conflicts of interest regarding the publication of this paper.

Acknowledgments

This study was supported by the National Natural Science Foundation of China (51379001) and the Open Fund of

State Key Laboratory of Hydraulics and Mountain River Engineering (SKHL1518).

References

- [1] E. M. Saiki and S. Biringen, "Numerical simulation of a cylinder in uniform flow: Application of a virtual boundary method," *Journal of Computational Physics*, vol. 123, no. 2, pp. 450–465, 1996.
- [2] A. L. F. Lima E Silva, A. Silveira-Neto, and J. J. R. Damasceno, "Numerical simulation of two-dimensional flows over a circular cylinder using the immersed boundary method," *Journal of Computational Physics*, vol. 189, no. 2, pp. 351–370, 2003.
- [3] D. K. Ofengeim and D. Drikakis, "Simulation of blast wave propagation over a cylinder," *Shock Waves*, vol. 7, no. 5, pp. 305–317, 1997.
- [4] M. Breuer, "Large eddy simulation of the subcritical flow past a circular cylinder: Numerical and modeling aspects," *International Journal for Numerical Methods in Fluids*, vol. 28, no. 9, pp. 1281–1302, 1998.
- [5] J. R. Meneghini, F. Saltara, C. L. R. Siqueira, and J. A. Ferrari Jr., "Numerical simulation of flow interference between two circular cylinders in tandem and side-by-side arrangements," *Journal of Fluids and Structures*, vol. 15, no. 2, pp. 327–350, 2001.
- [6] P. Hu, G. X. Wu, and Q. W. Ma, "Numerical simulation of nonlinear wave radiation by a moving vertical cylinder," *Ocean Engineering*, vol. 29, no. 14, pp. 1733–1750, 2002.
- [7] Y. L. Wu and C. Shu, "Application of local DFD method to simulate unsteady flows around an oscillating circular cylinder," *International Journal for Numerical Methods in Fluids*, vol. 58, no. 11, pp. 1223–1236, 2008.
- [8] S. Claus and T. N. Phillips, "Viscoelastic flow around a confined cylinder using spectral/hp element methods," *Journal of Non-Newtonian Fluid Mechanics*, vol. 200, pp. 131–146, 2013.
- [9] L.-C. Hsu, J.-Z. Ye, and C.-H. Hsu, "Simulation of Flow Past a Cylinder with Adaptive Spectral Element Method," *Journal of Mechanics*, vol. 33, no. 2, pp. 235–247, 2017.
- [10] I. Ginzburg and D. D'Humieres, "Multireflection boundary conditions for lattice Boltzmann models," *Physical Review E: Statistical, Nonlinear, and Soft Matter Physics*, vol. 68, no. 6, Article ID 066614, 2003.
- [11] F. J. Jiménez-Hornero, J. V. Giráldez, A. M. Laguna, S. J. Bennett, and C. V. Alonso, "Modelling the effects of emergent vegetation on an open-channel flow using a lattice model," *International Journal for Numerical Methods in Fluids*, vol. 55, no. 7, pp. 655–672, 2007.
- [12] H. Liu, J. G. Zhou, M. Li, and Y. Zhao, "Multi-block lattice Boltzmann simulations of solute transport in shallow water flows," *Advances in Water Resources*, vol. 58, pp. 24–40, 2013.
- [13] H. Liu and J. G. Zhou, "Lattice Boltzmann approach to simulating a wetting-drying front in shallow flows," *Journal of Fluid Mechanics*, vol. 743, pp. 32–59, 2014.
- [14] Y. Y. Yan and Y. Q. Zu, "Numerical simulation of heat transfer and fluid flow past a rotating isothermal cylinder - A LBM approach," *International Journal of Heat and Mass Transfer*, vol. 51, no. 9-10, pp. 2519–2536, 2008.
- [15] A. Rabienataj Darzi, A. H. Eisapour, A. Abazarian, F. Hosseinejad, and H. H. Afrouzi, "Mixed Convection Heat Transfer Analysis in an Enclosure with Two Hot Cylinders: A Lattice Boltzmann Approach," *Heat Transfer - Asian Research*, vol. 46, no. 3, pp. 218–236, 2017.
- [16] M. S. Longuet-Higgins and R. W. Stewart, "Radiation stresses in water waves; a physical discussion, with applications," *Deep-Sea Research and Oceanographic Abstracts*, vol. 11, no. 4, pp. 529–562, 1964.
- [17] B.-C. LIANG, H.-J. LI, and D.-Y. LEE, "Bottom Shear Stress Under Wave-Current Interaction," *Journal of Hydrodynamics*, vol. 20, no. 1, pp. 88–95, 2008.
- [18] F. Yang, Y. Li, L. Yang, and W. Du, "Modeling study of thermal discharge under current influence of wave and current," *Pearl River*, vol. 6, pp. 60–63, 2007.
- [19] Y. Lu, L. Zuo, H. Wang, and H. Li, "Two-dimensional mathematical model for sediment transport by waves and tidal currents," *Journal of Sediment Research*, vol. 6, pp. 1–12.
- [20] J. P. Le Roux, "Wave friction factor as related to the shields parameter for steady currents," *Sedimentary Geology*, vol. 155, no. 1-2, pp. 37–43, 2003.
- [21] J. G. Zhou and H. Liu, "Determination of bed elevation in the enhanced lattice Boltzmann method for the shallow-water equations," *Physical Review E: Statistical, Nonlinear, and Soft Matter Physics*, vol. 88, no. 2, Article ID 023302, 2013.
- [22] J. G. Zhou, *Lattice Boltzmann Methods for Shallow Water Flows*, Springer, Heidelberg, Germany, 2004.
- [23] Z. Zhong and K. H. Wang, "Modeling fully nonlinear shallow-water waves and their interactions with cylindrical structures," *Computers & Fluids*, vol. 38, no. 5, pp. 1018–1025, 2009.
- [24] S. Woo and L. Liu, "Finite element model for modified Boussinesq equations i: model development," *Journal of Waterway Port Coastal and Ocean Engineering*, vol. 130, pp. 1–16.

